Acta Materialia 177 (2019) 107–120

Contents lists available at ScienceDirect

Acta Materialia

journal homepage: www.elsevier.com/locate/actamat

Full length article

Helium irradiation induced ultra-high strength nanotwinned Cu with nanovoids

Cuncai Fan [a], Qiang Li [a], Jie Ding [a], Yanxiang Liang [b], Zhongxia Shang [a], Jin Li [a], Ruizhe Su [a], Jaehun Cho [a], Di Chen [c], Yongqiang Wang [d], Jian Wang [b], Haiyan Wang [a, e], Xinghang Zhang [a, *]

[a] School of Materials Engineering, Purdue University, West Lafayette, IN, 47907, USA
[b] Nebraska Center for Materials and Nanoscience, University of Nebraska-Lincoln, Lincoln, NE, 68583-0857, USA
[c] Department of Physics, University of Houston, Houston, TX, 77204-5005, USA
[d] Materials Science and Technology Division, Los Alamos National Laboratory, Los Alamos, NM, 87545, USA
[e] School of Electrical and Computer Engineering, West Lafayette, IN, 47907, USA

ARTICLE INFO

Article history:
Received 6 February 2019
Received in revised form 28 June 2019
Accepted 1 July 2019
Available online 3 July 2019

Keywords:
He irradiation
Nanotwinned cu
He bubbles
Micropillar compression
Radiation hardening

ABSTRACT

There are increasing studies that show nanotwinned (NT) metals have enhanced radiation tolerance. However, the mechanical deformability of irradiated nanotwinned metals is a largely under explored subject. Here we investigate the mechanical properties of He ion irradiated nanotwinned Cu with pre-existing nanovoids. In comparison with coarse-grained Cu, nanovoid nanotwinned (NV-NT) Cu exhibits prominently improved radiation tolerance. Furthermore, *in situ* micropillar compression tests show that the irradiated NV-NT Cu has an ultrahigh yield strength of ~1.6 GPa with significant plasticity. Post radiation analyses show that twin boundaries are decorated with He bubbles and thick stacking faults. These stacking fault modified twin boundaries introduce significant strengthening in NT Cu. This study provides further insight into the design of high-strength, advanced radiation tolerant nanostructured materials.

1. Introduction

Nuclear energy holds the promise as a reliable and economic next-generation source of electricity [1,2]. New concepts of advanced fusion and fission nuclear reactors require structural materials to perform reliably in extremely aggressive radiation environment (high dose and high temperature) [3–5]. Severe radiation damage often occurs in the core of nuclear power reactors where structural components are subjected to intense fluxes of energetic neutrons [6], resulting in a wide variety of defect clusters [7,8], such as dislocation loops [9–11], stacking fault tetrahedrons (SFTs) [12,13], and cavities (voids or bubbles) [14–16]. These defects typically cause significant degradation of mechanical properties for irradiated materials [17], including radiation induced hardening, fracture and embrittlement [18–22]. Design and manufacture of advanced materials that can resist damage at irradiation and mechanical extremes are grand challenges in nuclear energy industry [3,6,23,24].

As a classical model system, Cu has been the subject of numerous studies on both radiation damage effects [10,25–29] and mechanical properties [30,31]. The typical method to improve its mechanical and physical properties is through grain refinement [32]. For instance, nanocrystalline (NC) metals have significantly improved mechanical strength [33,34] and radiation tolerance [35,36] compared with their coarse-grained (CG) counterparts. However, NC metals tend to become brittle with decreasing grain sizes [33,34]. In addition, NC metals often have poor thermal stability, and radiation-induced grain-coarsening occurs even at room temperature [37]. An alternative approach to tune the mechanical properties of Cu is to utilize twin boundaries (TBs) [32,38]. It has been found that nanotwinned (NT) Cu exhibits ultrahigh strength and yet considerable ductility [30], as TBs are effective barriers for the transmission of dislocations [39]. Also NT Cu shows better thermal stability than NC Cu, and the annealed NT Cu still retains high hardness [40]. On the other hand, NT Cu proves to be more radiation tolerant than CG Cu in terms of lower defect density [41],

* Corresponding author.
E-mail address: xzhang98@purdue.edu (X. Zhang).

https://doi.org/10.1016/j.actamat.2019.07.003
1359-6454/

because TBs can effectively absorb, transport and finally eliminate a large number of radiation-induced defects [42–45]. The radiation tolerance of NT Cu can be enhanced further by introducing nanovoids (NVs) that act as 'storage bins' for interstitial defects [46,47]. Though several studies have recently been reported on the microstructural characterizations of irradiated NT Cu [41,46,48–50], its mechanical response to irradiation remains less well understood.

Heavy ion irradiation technique has been widely used as a surrogate to emulate neutron radiation damage effects on mechanical properties [51–53]. Nevertheless, the ion-beam-irradiated region is generally shallow on the surface with a penetration depth at micron scale [54,55]. To investigate mechanical properties of ion irradiated materials, small-scale mechanical testing techniques, such as nanoindentation [22], micro bending [56], tension [20] and compression [19], have been increasingly applied to nuclear materials [54,57–60]. In this study, we conduct *in situ* micropillar compression test inside a scanning electron microscope (SEM) to investigate the mechanical properties of He ion irradiated NV-NT and CG Cu. The results show that radiation induces less He bubbles in NV-NT Cu, and the irradiated NV-NT Cu has ultrahigh strength and remains significant plasticity.

2. Experimental

2.1. Materials and helium irradiations

High purity (99.995%) Cu films, ~ 2.6 μm thick, were deposited on HF-etched Si (110) substrates at room temperature using direct current magnetron sputtering technique. Before deposition, the chamber was evacuated to a base pressure < 8×10^{-8} torr. During deposition, ~ 1.2×10^{-3} torr Ar working pressure was used, and the deposition rate was controlled at ~ 0.6 nm/s.

The as-deposited Cu films were subsequently irradiated at room temperature with He ions at the Ion Beam Materials Lab, Los Alamos National Laboratory, USA. To produce a uniform irradiated region, three sets of He ion beams (with various energies of 50, 100 and 200 keV) were sequentially implanted into specimens. The corresponding ion doses are ~ 1×10^{16}, 2×10^{16} and 4×10^{16} ions/cm^2, respectively. Supplementary Figs. S1(a) and S1(b) show the profiles of radiation damage and He concentration along penetration depth (h), calculated using SRIM software with the Kinchin-Pease model [61]. The resultant radiation damage is 0.9 displacements-per-atom (dpa) on average, and almost uniformly distributed across a penetration depth of 200–630 nm. The average He concentration is 1.0 at. %, with a peak value of around 1.8 at. % when $h = 700$ nm. For comparison purposes, bulk CG Cu, annealed at 800 °C for 4 h, was polished and irradiated under the same conditions.

2.2. Micropillar compression

Micropillars were fabricated using the focused-ion-beam (FIB) technique, with a height of ~ 2.6 μm and a diameter of ~ 1.2 μm, following a generally preferred aspect ratio (height-to-diameter ration between 2:1 and 3:1) suggested for micro-compression experiment [62]. The test was conducted on a Hysitron PI 88 × R PicoIndenter inside an FEI Quanta 3D FEG SEM. During each compression process, two partial unloading segments were applied while maintaining a constant strain rate of 1×10^{-3} s^{-1}, and the maximum displacement was ~ 400 nm. To confirm the repeatability, at least three micropillars were compressed for each sample.

2.3. Microstructure characterization

The texture of as-deposited NV-NT Cu film was analyzed using an X-ray diffraction technique on a Panalytical Empyrean X'pert PRO MRD diffractometer with a Cu Kα_1 source. Plan-view (PV) and cross-sectional (CS) transmission electron microscopy (TEM) specimens were prepared by mechanical grinding and dimpling, followed by low-energy Ar ion milling. The annealed CG Cu was characterized by an optical microscope before irradiation. For the irradiated samples before and after compression tests, CS TEM specimens were prepared by FIB technique. All the TEM samples were examined on a FEI Talos 200 × TEM microscope operated at 200 kV.

3. Results

3.1. Radiation-induced evolution of microstructures

Supplementary Fig. S2 displays the texture analysis of the as-deposited Cu films. Fig. S2(a) is the θ-2θ XRD spectrum for the epitaxial Cu (111) film on the Si (110) substrate. The φ scan in Fig. S2(b) shows diffraction peaks from twin and matrix with nearly identical intensity, indicating the formation of high-density growth twins in the film. Fig. S2(c) schematically illustrates the film – substrate orientation relationships: Cu (111)//Si (110) and Cu $[01\bar{1}]$//Si $[1\bar{1}0]$ (matrix).

Fig. 1 displays the microstructural characterization of the materials for He irradiations. The PV TEM micrograph in Fig. 1(a) shows polygonal domains formed in as-deposited Cu film, and the inserted selected area diffraction (SAD) pattern confirms the formation of highly-textured Cu (111). The enlarged view in Fig. 1(b) shows abundant nanovoids (NVs) primarily located at domain boundaries. The CS TEM micrograph examined from Cu <110> zone axis in Figure 1(c) shows columnar domains along growth direction, and the inserted SAD pattern confirms the formation of growth twins. The enlarged view in Fig. 1(d) reveals high-density growth twins in columnar domains and the NVs (denoted by arrows) at domain boundaries. Statistic studies in Fig. 1(e–g) show the average domain size D_{NT}, void size d_V and twin spacing t, are approximately 115, 6 and 8 nm, respectively. The void number density N_V is also measured as $4.0 \pm 0.5 \times 10^{21}$/m^3. In contrast, the CG Cu sample contains large grains, ~ 43 μm in size, as shown in Fig. 1 (h) and (i).

Fig. 2 shows the microstructure of irradiated NV-NT Cu. The PV TEM images in Fig. 2(a)–(c) reveal the remaining NVs, radiation-induced defect clusters, and He bubbles. Fig. 2(d) is the panoramic cross-sectional view of the irradiated NV-NT Cu, superimposed with solid curve showing the calculated damage profile. The enlarged view of irradiated region in Fig. 2(e), taken along <110> zone axis, shows the retention of high-density nanotwins. The magnified views at different penetration depths in Fig. 2(f–i) reveal high-density He bubbles when $h = 400$ and 600 nm, but lower-density bubbles when $h = 200$ and 800 nm. In comparison, Fig. 3 shows the microstructure of He-irradiated CG Cu. The overview of a CS TEM micrograph in Fig. 3(a) shows the radiation-induced dislocation loops, and the magnified views in Fig. 3(b)–(e) show the He bubbles at various penetration depths. Note that there are more radiation-induced bubbles in CG Cu than in NV-NT Cu at the same penetration depth.

3.2. Mechanical properties of He ion irradiated NV-NT Cu

Fig. 4 compares the deformation behaviors for NV-NT and CG Cu micropillars under uniaxial compression. The load-displacement curves for all the compressed micropillars are compiled in

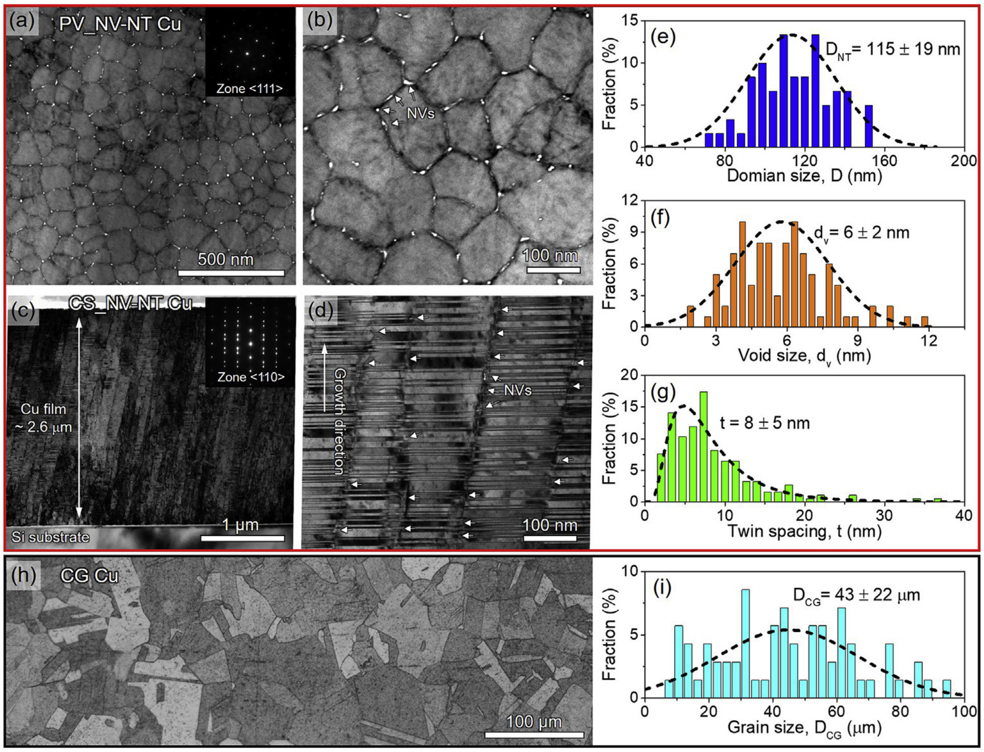

Fig. 1. Microstructures of as-deposited NV-NT Cu and annealed CG Cu before He irradiations. (a) and (b) Plan-view (PV) TEM images showing the (111) textured Cu film with polygonal domains and abundant nanovoids (NVs) at boundaries. (c) and (d) Cross-sectional (CS) TEM images showing high-density growth twins in columnar domains. Nanovoids are marked by arrows. (e-g) Statistic studies of domain size (D_{NT}), void size (d_V) and twin spacing (t) in NV-NT Cu. (h) Micrograph of coarse-grained (CG) Cu. (i) The grain size (D_{CG}) distribution of CG Cu.

Fig. 4(a). The as-received CG Cu was soft and the load-displacement curves have long plateaus, and numerous inclined discrete slip bands formed on the surface after deformation, as shown in Fig. 4(b1-b5). After He ion irradiation, the load increased moderately with displacement. Interestingly, the irradiated CG pillars first experienced barreling deformation near the base part where the material was little irradiated, while the heavily irradiated region on the top portion remained nearly undeformed, as shown in Fig. 4(c1-c5). In comparison, the pillars of as-deposited and irradiated NV-NT Cu were much harder, and they both experienced substantial plastic deformations primarily at the pillar tops, as shown in Fig. 4(d1-d5) and Fig. 4(e1-e5). More details on the evolution of pillar morphology during *in-situ* micropillar compression tests of the four types of specimens can be found in supplementary videos SV1-SV4.

It should be noted that the pillars were deformed nonuniformly, so the compressive stress-strain curves cannot be directly calculated using the typical methodology reported in previous studies [63]. To address the issue and to measure the local stress more accurately, the true compressive stress is calculated by dividing the load by corresponding instantaneous cross-sectional area directly obtained from the sequential snapshots of *in-situ* SEM videos. Details on the true stress measurement can be found in Supplementary Figs. S3 and S4.

The calculated stress-displacement curves for all the compressed pillars are compiled and plotted in Fig. 5. The stress-displacement curves for as-received (AR) Cu pillars (solid lines) show nearly elastic initial loading, followed by long stress plateaus with numerous discrete strain bursts (Fig. 5(a)). The true stresses for irradiated (IR) CG pillars were calculated at two positions, the irradiated pillar top (solid data points) and the unirradiated region − the middle portion of the pillar (shown as open data points). The open data points match well with the solid lines, while the solid data points show considerable hardening with increasing displacement compared to unirradiated CG Cu. Furthermore, for as-deposited (AD) or irradiated (IR) NV-NT Cu, only the pillar tops experienced plastic deformations. The true stresses for irradiated NV-NT Cu (solid data points) and as-deposited specimens (open data points) are compared in Fig.5 (b). The irradiated NV-NT Cu has greater yield strength than the as-deposited counterparts. After yielding, both types of NV-NT Cu pillars exhibited slight hardening followed by significant softening. Such softening is ascribed to the internal microstructural change that will be analyzed further in the following section.

In order to quantify the radiation-induced hardening, two stresses are defined and marked in Fig. 5, yield stress σ_Y and ultimate compressive stress σ_U. Table 1 summarizes the values of σ_Y and σ_U for all the compressed pillars. The radiation-induced strengthening $\triangle\sigma^{Irrad}$ for NV-NT Cu thus was calculated by comparing the σ_Y between the as-deposited and irradiated specimens. For CG Cu, however, each pillar may be a single-crystal-like pillar and thus has a different crystallographic orientation that may affect the yield strength. To avoid such an orientation effect, the $\triangle\sigma^{Irrad}$ for irradiated CG Cu pillar is calculated by the subtraction of its σ_Y measured at the unirradiated (middle) section of the pillar from σ_U measured at its irradiated pillar top, as marked in Fig. 5(a). The strength increment calculations are summarized in Table 2 and will be discussed later in more detail.

3.3. Post compression analyses

To investigate the deformation mechanisms of NV-NT Cu, post-

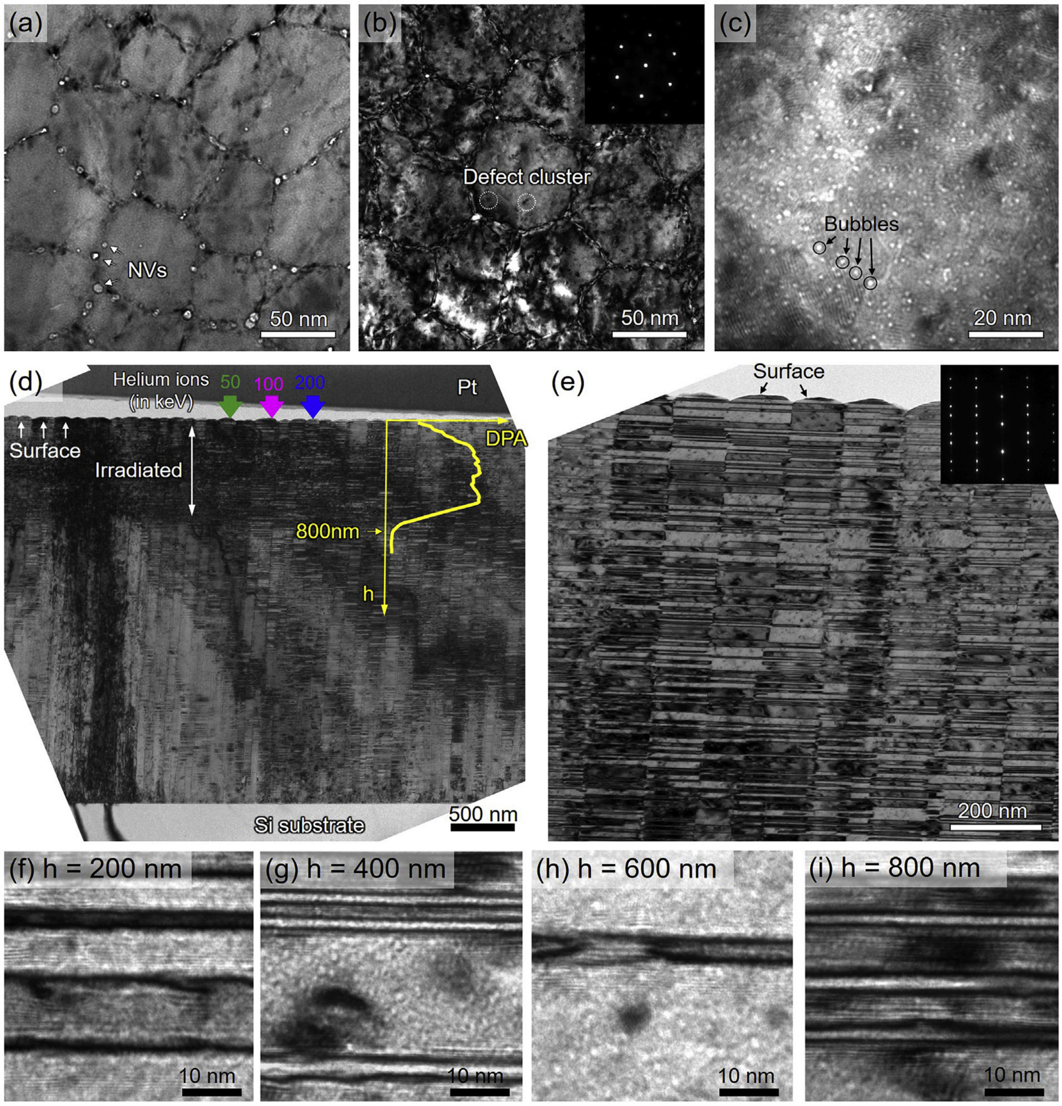

Fig. 2. Microstructure of He ion irradiated NV-NT Cu. (a)-(c) Plan-view TEM images showing surviving NVs at domain boundaries and radiation-induced defect clusters, as well as He bubbles. (d) Cross-sectional overview of the irradiated specimen superimposed with the depth-dependent DPA profile. (e) Enlarged view of the irradiated region close to film surface showing defect clusters. (f-i) Radiation-induced He bubbles at various radiation depth.

compression TEM examinations were performed. Fig. 6(a) displays an overview of the area near pillar top. The TEM sample was tilted to Cu <110> zone axis for the undeformed region where high-density growth twins can be clearly seen, while in the plastically deformed region most of the twins have been removed. The SAD pattern for the deformed region in Fig. 6(b) indicates the crystal rotation induced by heavy plastic deformation. In comparison, the SAD pattern for undeformed region in Fig. 6(c) shows a typical symmetrical twin pattern, together with extra spots (marked by circles) arising from ITBs. The corresponding dark-field (DF) TEM micrograph in Fig. 6(d) confirms the removal of growth twins in the plastic deformation region. As shown in Fig. 6(e), the enlarged view of box (e) in Fig. 6(a) denotes a sharp boundary (dotted line) between the deformed and undeformed region. High-density dislocations were observed along the boundary. The enlarged view in Fig. 6(f) shows several remaining TBs that have been greatly distorted in the plastic deformation region.

Somewhat different microstructures have been observed in the deformed pillar of He-irradiated NV-NT Cu, as shown in Fig. 7. The overview TEM micrograph in Fig. 7(a) shows the substantial plastic deformation confined near the pillar top. The SAD pattern in Fig. 7(b) indicates the retention of twins in the deformed region, and there is much less crystal reorientation than that in the as-deposited NV-NT Cu. Compared with the SAD pattern from undeformed region in Fig. 7(c), there are no extra spots from ITBs in the plastic deformed pillar top. The retention of nanotwins in the deformed region is also confirmed by the corresponding DF TEM image in Fig. 7(d). The enlarged view in Fig. 7(e) also denotes the sharp boundary between deformed and undeformed region, and the enlarged view in Fig. 7(f) shows numerous He bubbles and the stacking faults (SFs) along the remaining TBs in the plastic deformation region.

4. Discussion

4.1. Irradiation-induced He bubbles and lattice expansion

At room temperature, He atoms are essentially insoluble in metals [64,65], and they can easily migrate and combine with radiation-induced vacancies to form bubbles [66,67]. It has been

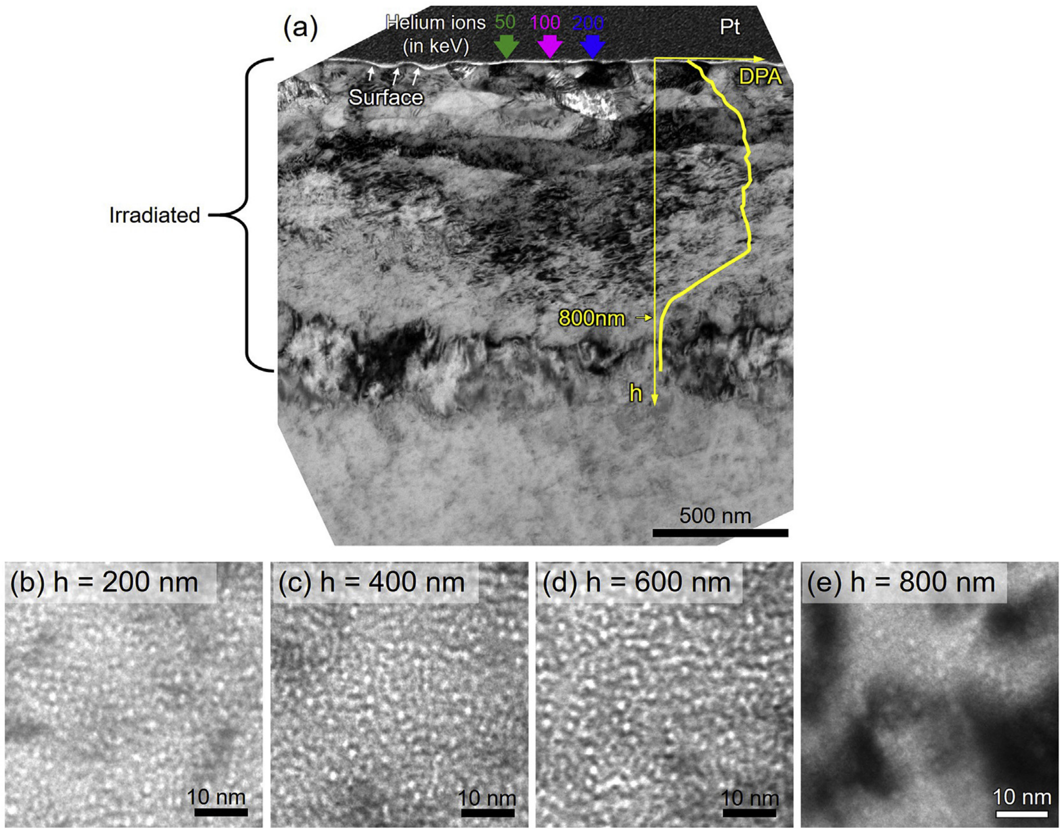

Fig. 3. Microstructure of He ion irradiated CG Cu. (a) Cross-sectional TEM image showing the overview of irradiated Cu, superimposed with the depth-dependent DPA profile. (b-e) TEM micrographs displaying radiation-induced He bubbles at various depths.

shown that precipitated He bubbles can significantly distort crystal lattices and cause substantial lattice expansion [68]. In the current study, more bubbles are produced in CG Cu than in NV-NT Cu, as shown in Figs. 2 and 3. The variation of bubble density with increasing penetration depth shown in Supplementary Fig. S5(a) is in good agreement with calculated He concentration profile (black curve). Note that over the depth of 200–600 nm, the bubble density, ρ_B, remains a constant, about $2.2 \pm 0.2 \times 10^{24}/m^3$ for CG Cu, twice larger than that in the irradiated NV-NT Cu, $1.2 \pm 0.1 \times 10^{24}/m^3$. The histograms in Supplementary Fig. S5(b) show the bubble size (d_B) varies from 1.0 to 2.5 nm in both cases regardless of the radiation depth, and they have nearly the same average bubble size of ~1.5 nm.

The lattice expansion is evidenced by the variation of SAD patterns, as shown in Supplementary Fig. 5(c1) and (c2) examined along <110> zone axis over the depth of 200–600 nm. The lattice expansion is calculated to be 1.83 ± 0.76 (%) for CG Cu, much larger than that in NV-NT Cu, 0.84 ± 0.09 (%). The reduced lattice expansion in NV-NT Cu may be related to the pre-existing NVs. Unlike our previous studies that showed preexisting NVs could shrink rapidly after absorbing the interstitials induced by 1 MeV Kr ion irradiations [46,47,69], most of the preexisting nanovoids survived He irradiation in the current study. The underlying mechanism is attributed to the effect of He on the kinetics of void growth or shrinkage [67]. With the further addition of He atoms into NVs, the void internal pressure increases until it reaches a stable state. According to the proposed critical bubble model (CBM) [70], the shrinkage rate for nanoscale voids will decrease prominently in the presence of internal He pressure. From another point of view, when the He-filled NVs capture interstitials, the internal He pressure will build up even further, and thus He once absorbed by voids will reduce the driving force for NVs to absorb interstitials. Meanwhile, the NVs can reduce He bubble density and alleviate lattice expansion by trapping a large number of Helium atoms. Conversely, for CG Cu, nearly all He atoms may reside in bubbles, leading to higher bubble density and more lattice expansion. He ion irradiation induced lattice expansion has been observed previously in Cu/V nanolayers, and the magnitude of He bubble induced lattice expansion appears to decrease with decreasing individual layer thickness [68].

4.2. Mechanical properties of nanotwinned Cu

It is well known that the strength of micropillars shows a strong size-dependence (extrinsic size effect) [63], and there is a critical pillar diameter beyond which the extrinsic size effect is insignificant, that is the measured properties of pillars are similar to those of bulk materials [71,72]. It is worth pointing out that the critical pillar size depends on the intrinsic microstructure characteristics and their interactions with mobile dislocations [73]. Previous micro-compression studies on perfect single-crystal Cu revealed that the size effect is exerted on all the micropillars with diameters of less than several μm [74], presumably because of the absence of dislocation sources and obstacles [75]. The flow stress of CG Cu is ~ 0.2 GPa, comparable to those reported in the literature [74]. Furthermore, for the irradiated materials containing high-density defect clusters, the transition diameter of pillars of single-crystal Cu pillars has been experimentally estimated to be ~ 400 nm [73,76]. The measured strengths of irradiated Cu in the current study are based on the compression tests on micropillars with 1.2 μm in diameter. Therefore, our measured values can be reasonably compared with previous studies and will be discussed

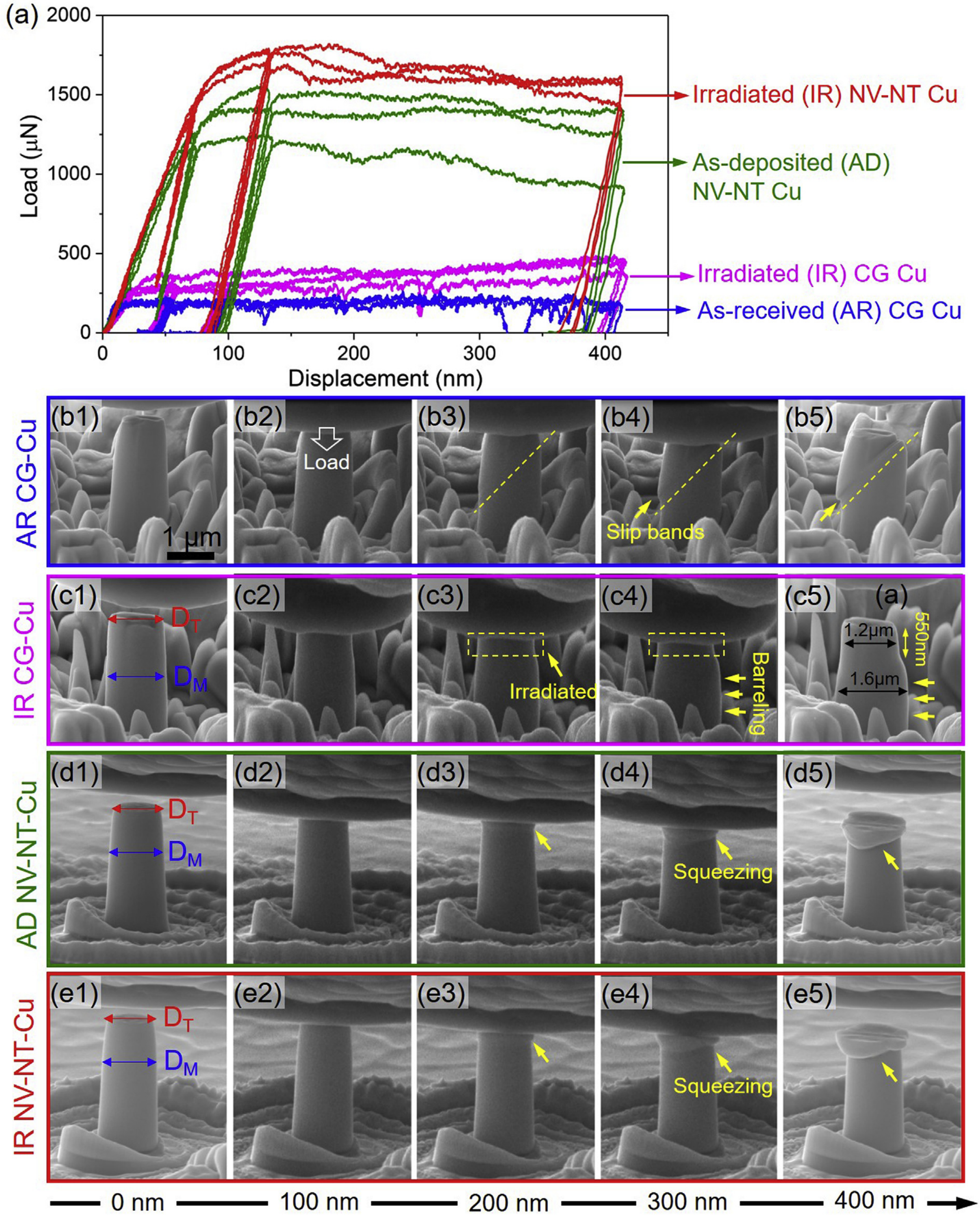

Fig. 4. *In situ* micropillar compression studies on CG Cu and NV-NT Cu before and after He ion irradiations. See supplementary videos SV1-SV4 for details. (a) Compilation of load-displacement curves of various specimens under compression. (b1-e5) SEM snapshots of pillars compressed to various displacements; (b1-b5) Formation of typical slip bands in as-received (AR) CG Cu; (c1-c5) Micrographs showing base barreling and deformation at unirradiated region in irradiated (IR) CG Cu. (d1-d5) and (e1-e5) Severe squeezing and extrusion on pillar top for as-deposited (AD) and irradiated (IR) NV-NT Cu, respectively. D_T and D_M in (c1), (d1) and (e1) mark the diameters of pillar top and middle, used for compressive stress measurement, as shown in Supplementary Figure S3 and S4.

later in detail.

For NT Cu, experiments and simulations reveal that twin-spacing t plays an important role in determining their mechanical properties [31,77]. Fig. 8 compiles the yield strength σ_Y versus $t^{-0.5}$ for previously reported studies on NT Cu [30,31,39,40,78–84]. When $t > 15$ nm, the strength is dominated by the resistance of TBs against slip transmission of dislocations, and σ_Y follows the conventional Hall-Petch (H–P) relationship:

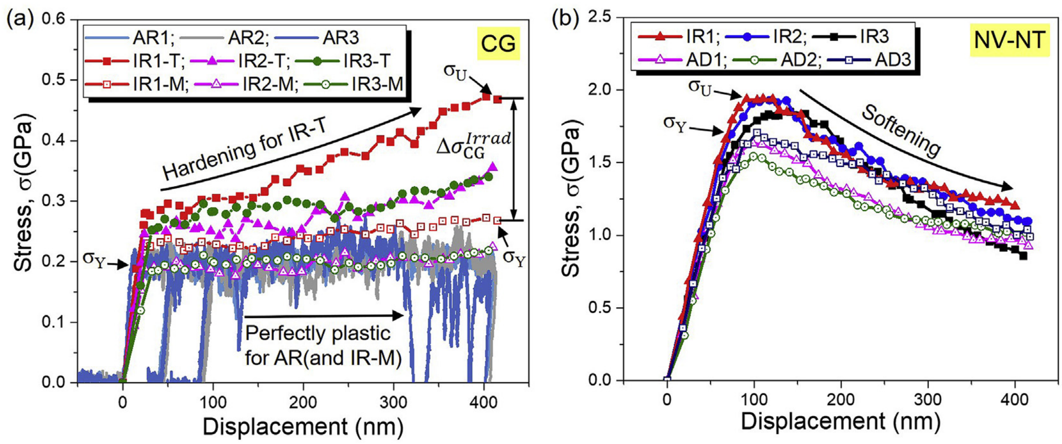

Fig. 5. Stress-displacement curves of (a) CG and (b) NV-NT pillars. AR: as-received; IR: Irradiated; IR-T: Irradiated pillar top; IR-M: Irradiated pillar middle; AD: as-deposited. Three pillars (marked as 1, 2 and 3) were compressed for each sample. In (a), AR-CG Cu pillars are perfectly plastic with little hardening, while the IR-CG Cu pillars exhibit considerable hardening at top portion (irradiated region). (b) The softening of top stresses for all the compressed NV-NT Cu pillars (AD or IR). See Supplementary Figure S3 and S4 for stress measurement.

Table 1
Yield stress σ_Y and ultimate stress σ_U for all the compressed pillars, defined and measured based on the local stress-displacement curves in Fig. 5. AR – As-received; IR – Irradiated; AD – As-deposited.

Material	Sample		σ_Y(GPa)	σ_U(GPa)
CG Cu	AR	1	0.19 ± 0.03	0.19 ± 0.03
		2	0.20 ± 0.03	0.20 ± 0.03
		3	0.19 ± 0.05	0.19 ± 0.05
	IR	1	0.25 ± 0.03	0.47 ± 0.01
		2	0.20 ± 0.02	0.35 ± 0.01
		3	0.20 ± 0.02	0.34 ± 0.01
NV-NT Cu	AD	1	1.32 ± 0.10	1.68 ± 0.02
		2	1.21 ± 0.13	1.63 ± 0.01
		3	1.21 ± 0.10	1.52 ± 0.01
	IR	1	1.65 ± 0.20	1.94 ± 0.02
		2	1.59 ± 0.16	1.84 ± 0.02
		3	1.56 ± 0.08	1.85 ± 0.01

$$\sigma_Y = \sigma_0 + k_{TB} t^{-0.5} \tag{1}$$

where σ_0 is the lattice friction stress, ~ 100 MPa, and k_{TB} is a material constant. However, when $t < 15$ nm, the size dependent variation of σ_Y appears to be more influenced by texture [82]. On the one hand, for polycrystalline NT Cu with equiaxed grains (Eq-NT Cu), softening occurs with decreasing t, which is governed by the dislocation nucleation at grain boundary-twin intersections [77]. The softening behavior can be described by dislocation-nucleation-controlled (DNC) mechanism [77] that shows:

$$\sigma_Y = \frac{\Delta U}{SV^*} - \frac{k_B T}{SV^*} \ln\left(\frac{d\nu_D}{t\dot{\varepsilon}}\right) \tag{2}$$

where ΔU is the activation energy, S is a factor presenting local stress concentration and geometry, V^* is the activation volume, k_B and T are the Boltzmann constant and temperature, d is the grain size, ν_D is the Debye frequency, and $\dot{\varepsilon}$ is the macroscopic strain rate.

On the other hand, for the preferentially (111) textured NT Cu with columnar grains (Col-NT Cu), its σ_Y continues to increase slightly with decreasing t [82]. Considering most TBs are parallel with each other and normal to the loading axis under compression, the strength variation of Col-NT Cu is better described by confined layer slip (CLS) model [85]:

$$\sigma_Y = \sigma_0 + \gamma \frac{\mu b}{t} \ln\left(\frac{\eta t}{b}\right) \tag{3}$$

where μ is the shear modulus, b is the magnitude of the Burgers vector, and γ and η are material constants. For Cu, $\mu = 48$ GPa, $b = 0.256$ nm, $\eta = 0.16$ and $\gamma = 0.40$ [82].

According to the CLS model, dislocations are confined by adjacent TBs, plastic deformation occurs by dislocation bowing between TBs [82,85]. In addition, the model predicts the upper limit of strength for NT Cu is ~1.2 GPa, when $t = be/\eta \approx 4$ nm, where e is the nature constant. In reality, if $t < 4$ nm, the ultrafine NT Cu is most likely to suffer from significant detwinning, driven by strong twin-twin interactions [86]. The strongest NT Cu reported to date has a flow stress of 1.2 GPa, with a twin spacing of ~ 4 nm [79]. In our work, the NV-NT Cu has an average twin spacing of 8 nm, but its yield stress σ_{NV-NT} is ~1.25 ± 0.06 GPa (see Table 1). Such a high strength arises from two contributions: TBs and nanovoids. The contribution from TBs σ_{NT} is estimated to be 1.09 GPa by substituting $t = 8$ nm into Equation (3), while the strengthening from the nanovoids ($\Delta\sigma_V$) and can be described by the proposed dispersed barrier model [17]:

$$\Delta\sigma_V = \alpha_V M \mu b \sqrt{N_V d_V} \tag{4}$$

where α_V is a parameter depending on the average barrier strength of the irradiation-induced defect clusters, ~1 for voids [87,88], M is the

Table 2
Comparisons of radiation-induced microstructure evolution and strength increment, between CG Cu and NV-NT Cu. d_B – bubble size; ρ_B – bubble density; d_D – dislocation loop size; ρ_D– dislocation loop density. $\Delta\sigma_B + \Delta\sigma_D$ is the calcualted value using Euqation (5) and (6), and $\Delta\sigma^{Irrad}$ is the measured value from Table 1.

Material	Bubbles		Dislocation loops		Strength increment	
	d_B(nm)	$\rho_B(1\times10^{24}/\text{m}^3)$	d_D(nm)	$\rho_D(1\times10^{22}/\text{m}^3)$	$\Delta\sigma_B + \Delta\sigma_D$(GPa)	$\Delta\sigma^{Irrad}$(GPa)
CG Cu	1.5 ± 0.3	2.3 ± 0.2	9 ± 4	2.0 ± 0.5	~0.22	~0.17 ± 0.04
NV-NT Cu	1.5 ± 0.3	1.2 ± 0.1	6 ± 2	1.2 ± 0.4	~0.14	~0.35 ± 0.05

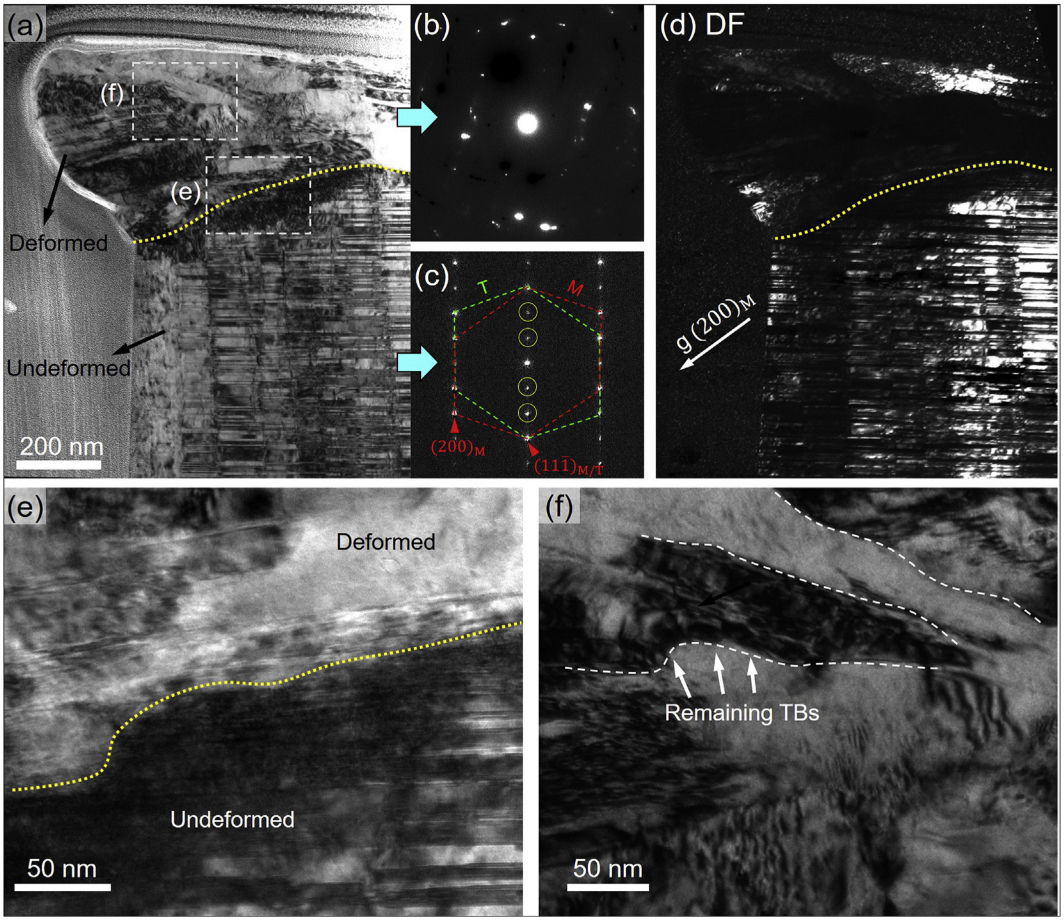

Fig. 6. The microstructure of a compressed pillar for as-deposited NV-NT Cu. (a) The bright-field TEM image of the deformed pillar showing the detwinning in the plastically deformed region. (b) and (c) The SAD patterns from deformed and undeformed regions, respectively. (d) Corresponding DF TEM image showing lower twin density in the deformed region. (e) and (f) Enlarged views of the squares in (a).

Taylor factor, defined as the ratio of the uniaxial stress to the resolved shear stress, and is estimated as 3.674 when the uniaxial strength is along the <111> direction for face-centered-cubic materials [89]; μ and b are shear modulus and Burgers vector as defined in Equation (3); N_V and d_V are void density and size. Setting $\alpha_V = 1$, $M = 3.674$, and substituting $N_V = 4.0 \pm 0.5 \times 10^{21}/\mathrm{m}^3$ and $d_V = 6 \pm 2$ nm into Equation (4) gives $\Delta\sigma_{NV} = 0.22 \pm 0.05$ GPa. Hence the nanovoids reasonably account for the extra strengthening (0.16 ± 0.06 GPa) observed in NV-NT Cu comparing to NT Cu without nanovoids as shown in Fig. 8. In addition, as shown in Table 1, after He irradiations, the yield strength of NV-NT Cu can increase further to 1.60 ± 0.05 (GPa). The strength increment $\Delta\sigma^{Irrad}$ (0.35 ± 0.05 GPa) caused by irradiation must be closely associated with radiation damage, which will be discussed in detail in the following section.

4.3. Radiation-induced hardening

Strengthening in irradiated metals is caused by the production of various defects and their interactions with mobile dislocations [51]. In He-irradiated metals, the primary defects are dislocation loops and He bubbles [90]. For dislocation loops that are classified as strong obstacles, their contribution to strengthening can also be described by the dispersed barrier model [17]:

$$\Delta\sigma_D = \alpha_D M\mu b\sqrt{N_D d_D} \tag{5}$$

where α_D is the parameter indicating the average barrier strength of the irradiation-induced dislocation loops, approximately 0.2 in Cu [91]; N_D and d_D are the respective density and size of dislocation loops. M, μ and b are the same parameters as defined in Equation (4).

For He bubbles, the magnitude of their barrier resistance appears to be dependent on internal pressure [68,92]. Fig. 9 compares the high-resolution TEM (HRTEM) micrographs of nanoscale twins in NV-NT Cu before and after He irradiations. As-deposited NV-NT Cu has nearly perfect (pristine) CTBs in Fig. 9(a) and (c). In contrast, the CTBs in irradiated NV-NT Cu are decorated with He bubbles in Fig. 9(b) and SFs in Fig. 9(d). Also, many of the bubbles are hexagonally faceted rather than spherical, indicating their low internal pressure [93]. It has been demonstrated that under-pressurized He bubbles are weak obstacles to mobile dislocations [92] or crack propagation [56]. To describe the weak strengthening arising from under-pressurized bubbles, $\Delta\sigma_B$, an alternative relationship was developed by Friedel-Kroupa-Hirsch (FKH) [94]:

$$\Delta\sigma_B = \frac{1}{8}M\mu b d_B N_B^{2/3} \tag{6}$$

where M, μ and b are the same parameters defined in Equation (4); d_B and N_B are bubble size and density.

Table 2 compares the size and density of He bubbles and dislocation loops for irradiated CG Cu and NV-NT Cu over the penetration depth of 200–600 nm. These measurements were

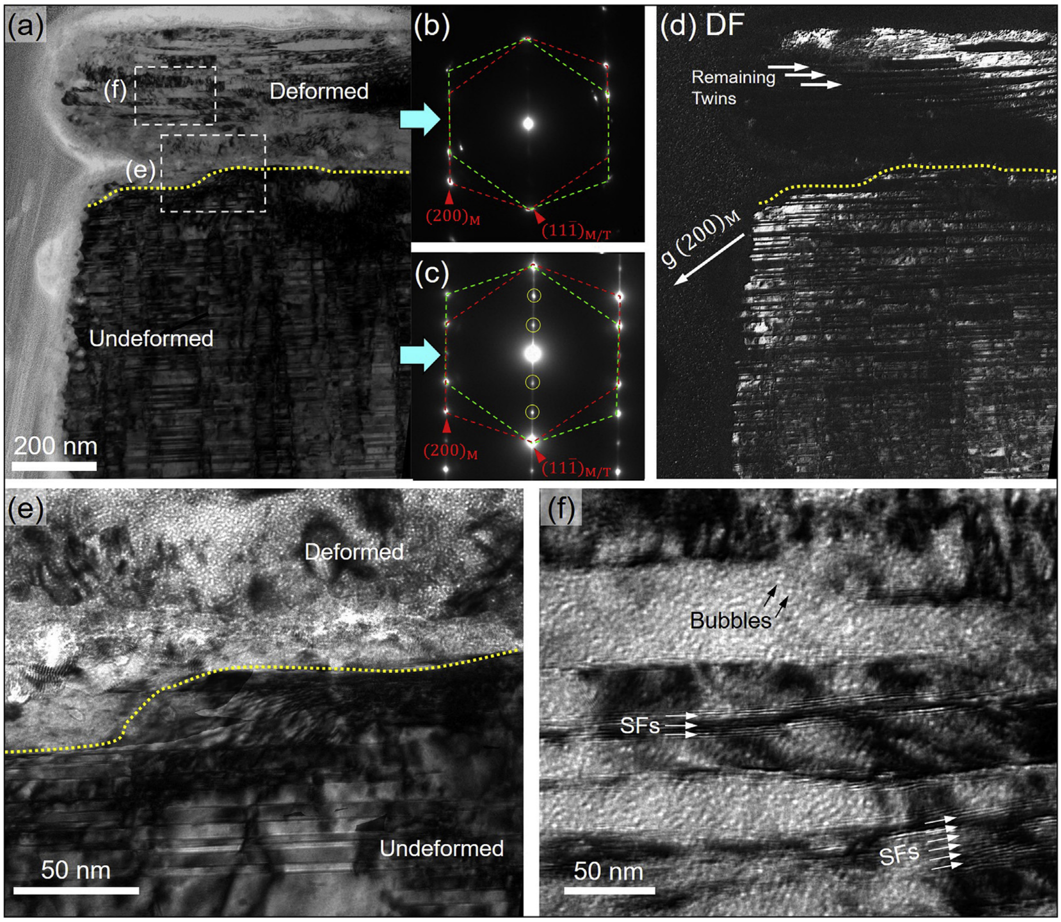

Fig. 7. Deformed microstructure of a compressed pillar for He-irradiated NV-NT Cu. (a) The bright-field TEM image of the plastically deformed region. (b) and (c) The SAD patterns from deformed and undeformed regions, respectively. The deformed region has CTBs, but little sign of ITBs. (d) Corresponding DF TEM image showing the withholding of twins in the deformed region. (e) and (f) Enlarged views of the marked boxes in (a) showing formation of He bubbles and SFs along deformed TBs.

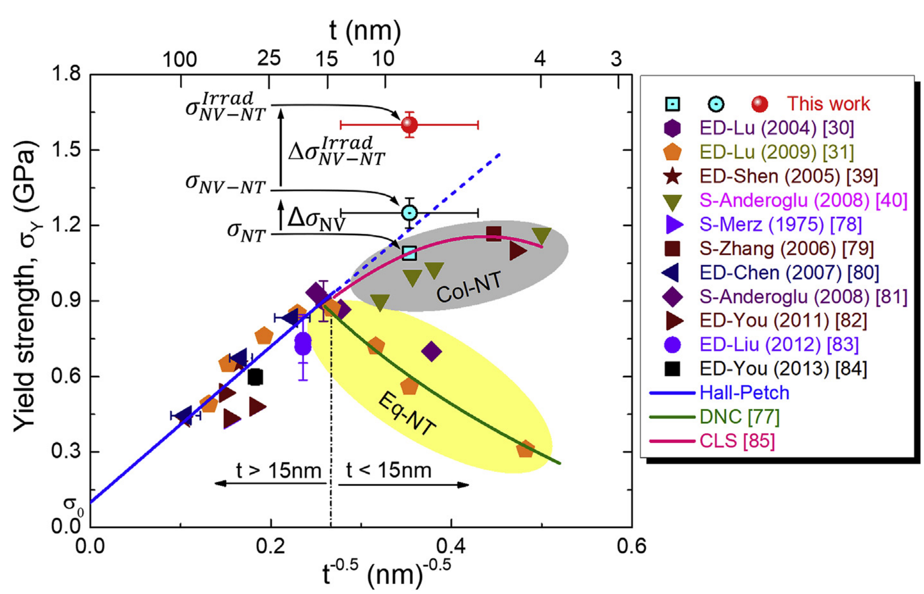

Fig. 8. Comparison of yield strength σ_Y of He-irradiated NV-NT Cu with previous studies synthesized by electrodeposition and sputtering [30,31,39,40,78-84]. σ_Y shows a strong dependence on twin spacing (t) and reaches a maximum value ~ 1.2 GPa at $t \approx 4$ nm, while He irradiation can increase the yield strength of NT Cu to 1.6 GPa when $t \approx 8$ nm. The strength data points are obtained from compressive (this work) and tensile tests or estimated as 1/3 of hardness. S, sputtering; ED, electrodeposition; DNC, dislocation-nucleation-controlled [77]; CLS, confined layer slip [85].

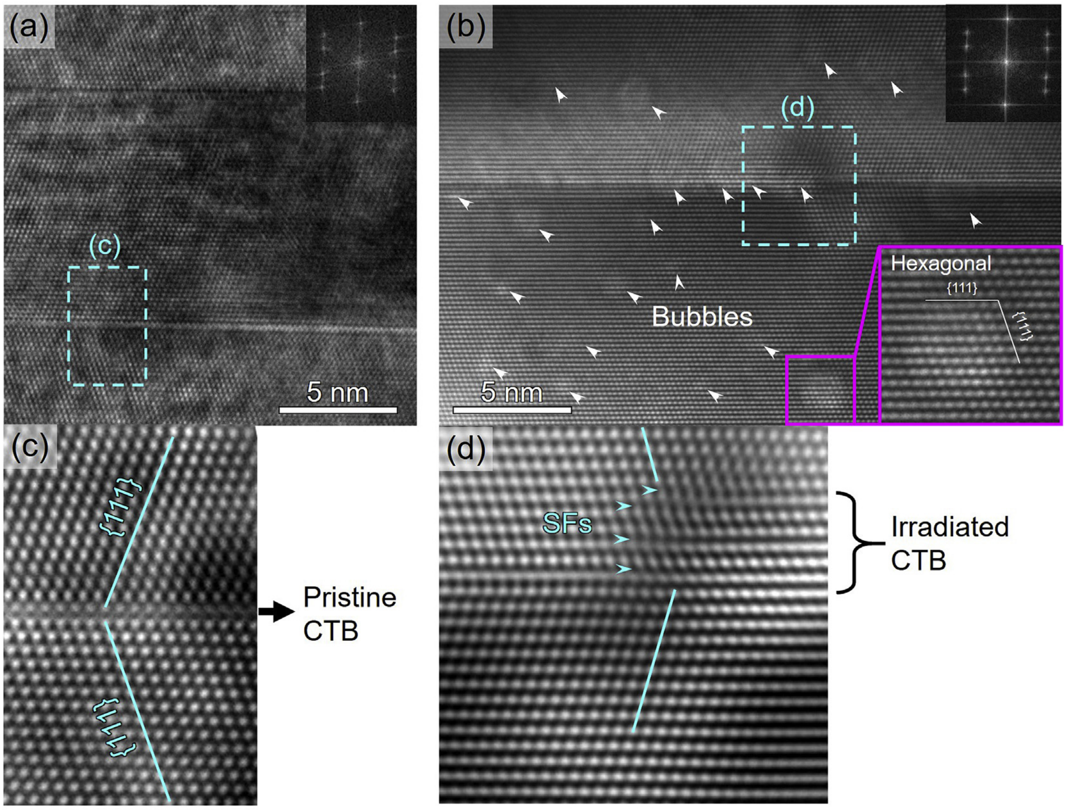

Fig. 9. HRTEM images comparing the microstructures of pristine and He-irradiated CTBs. (a) Typical nanotwins in as-deposited NT Cu. (b) He-irradiated NT Cu with abundant bubbles distributed in the lattice and along CTBs. The inset shows an HRTEM image of a hexagonally faceted He bubble. (c) Enlarged view of the square in (a) showing a narrow nearly perfect CTB. (d) The enlarged view of the square in (b) showing several SFs along a CTB in irradiated NT Cu.

obtained from our TEM analyses (see Figs. 2 and 3 for examples), and more detailed information can be found in Supplementary Figs. S5 and S6. Especially, an average value of Taylor factor M (~ 3.06) was used for calculating the irradiation-induced strength increase in polycrystalline CG Cu[95], while a higher value of 3.674 was used in the case of highly-textured NV-NT Cu (111) [89]. The measured and calculated strengthening are summarized in Table 2. Note that, although the irradiated NV-NT Cu contains a lower density of bubbles and dislocation loops, it experiences a higher strength increment, $\Delta\sigma^{Irrad}$, than irradiated CG Cu does.

The radiation-induced strengthening in CG Cu, $\Delta\sigma_{CG}^{Irrad}$, arises from both the weak obstacles (He bubbles) and strong obstacles (dislocation loops). Its total increment in this scenario is given as [51]:

$$\Delta\sigma_{CG}^{Irrad} = \Delta\sigma_B + \Delta\sigma_D \tag{7}$$

Using Equations (5) and (6), $\Delta\sigma_B$ and $\Delta\sigma_D$ are calculated as ~ 0.12 GPa and 0.10 GPa, respectively, hence the overall strengthening $\Delta\sigma_{CG}^{Irrad}$ in CG Cu is estimated as ~ 0.22 GPa. Based on the micropillar compression test in Fig. 4, the measured value of $\Delta\sigma_{CG}^{Irrad}$ is 0.17 ± 0.04 GPa (see Table 1). But considering the pillar base (the unirradiated region) yields first as shown in Fig. 4(c3), the true strength increment in the top irradiated region should be slightly higher than 0.17 GPa, and it is expected to be comparable with the calculated value.

We now attempt to interpret the radiation-induced strengthening in NV-NT Cu. Before irradiation, the strength of NV-NT Cu can be estimated as:

$$\sigma_{NV-NT} = \sigma_0 + \sigma_{NV} + \sigma_{TB} \tag{8}$$

where σ_0 is the lattice friction; σ_{NV} and σ_{TB} are the contributions from NVs and TBs, respectively. After He irradiations, the strength of NV-NT Cu is determined by:

$$\sigma_{NV-NT}^{Irrad} = \sigma_0 + \sigma_{NV}^* + \sigma_{TB}^* + \Delta\sigma_B + \Delta\sigma_D \tag{9}$$

where σ_{NV}^* refers to the He-filled NVs, and σ_{TB}^* refers to the irradiation modified TBs. Combining Equations (8) and (9) yields the irradiation induced strengthening, $\Delta\sigma_{NV-NT}^{Irrad}$, in NV-NT Cu:

$$\Delta\sigma_{NV-NT}^{Irrad} = \Delta\sigma_B + \Delta\sigma_D + (\sigma_{NV}^* - \sigma_{NV}) + (\sigma_{TB}^* - \sigma_{TB}) \tag{10}$$

As shown in Table 2, the measured value of $\Delta\sigma_{NV-NT}^{Irrad}$ from pillar compression tests is 0.35 ± 0.05 GPa. However, the calculated values of $\Delta\sigma_B$ and $\Delta\sigma_D$, from Equations (5) and (6), add up to only ~ 0.17 GPa, insufficient to account for the measured strengthening in NV-NT Cu. The extra strengthening must come from the irradiation modified NVs and TBs, that is the last two terms on the right side of Equation (10). Supplementary Fig. S7 compares the plan-view TEM images of as-deposited and irradiated NV-NT Cu, and shows little change on the size or number density of NVs after He irradiation. In other words, the contribution of the third term (irradiation modified NVs) in Equation (10) to strengthening maybe insignificant. Therefore, the last term, arising from the irradiation modified TBs, may play a primary role in the irradiation hardening in NV-NT Cu. Furthermore, as shown in Fig. 9, the irradiated TBs are decorated with bubbles and SFs, thus these defective TBs may be stronger barriers against trespassing of dislocations than pristine

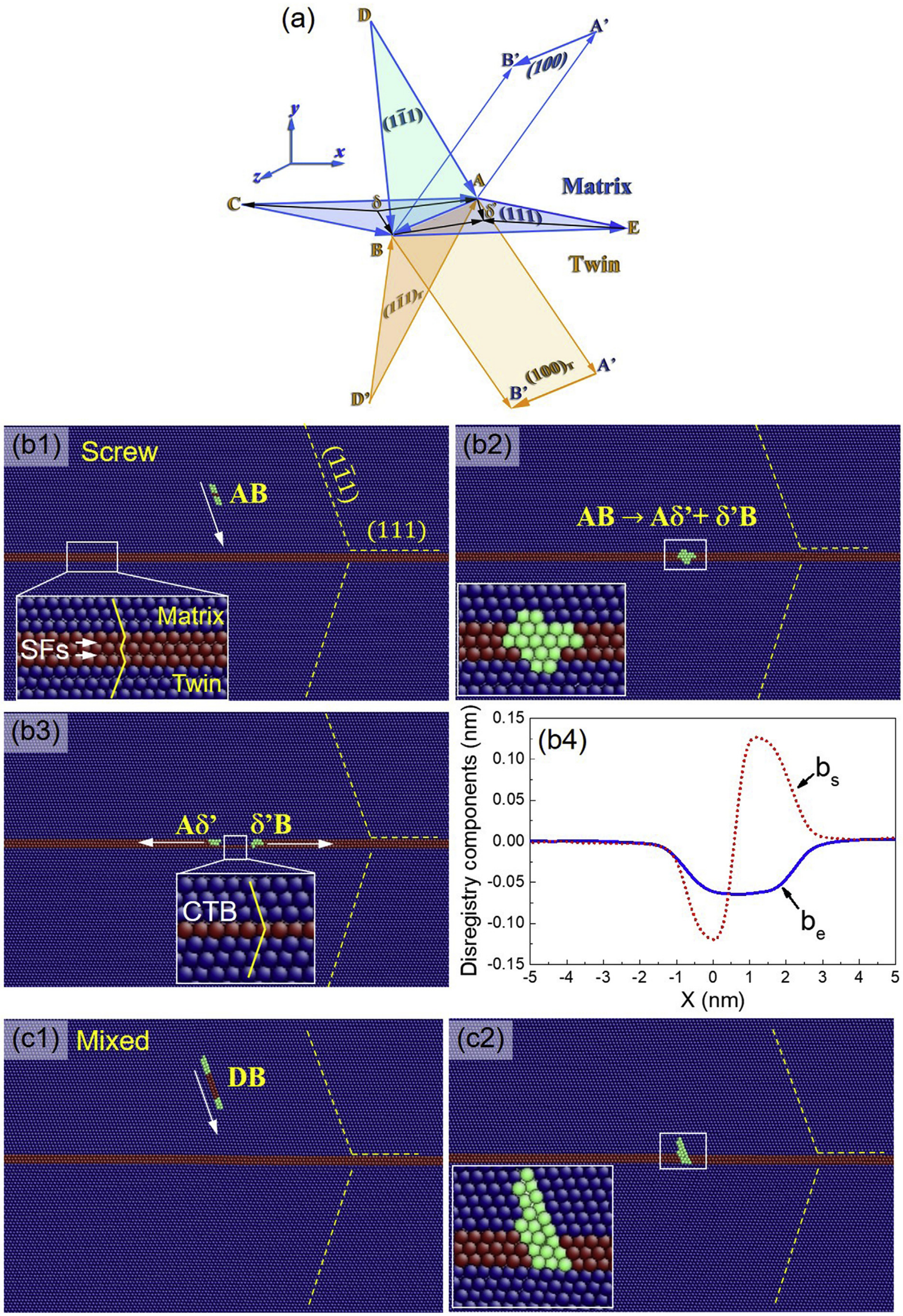

Fig. 10. MD simulations on dislocation-SF interactions in twin plan. (a) Thompson tetrahedron notation demonstrating the orientation relation and several slip systems between a twin and the matrix. (b1-b3) MD snapshots illustrating the dissociation of a screw dislocation **AB** into two partials (**Ad'** and **d'B**). (b4) The corresponding disregistry plot of the dissociated structure in (b3). (c1-c2) MD snapshots illustrating a mixed dislocation **DB** interacting with SFs. (See supplementary videos, SV5 and SV6).

(sharp) TBs in as-deposited NV-NT Cu. Such an aspect will be confirmed further by molecular dynamic (MD) simulations in the following section.

4.4. Deformation mechanisms

Based on experiments and discussions above, we finally address the deformation mechanisms of Cu under uniaxial compression. Previous micro-compression test on non-tapered pillars of electrodeposited polycrystalline Cu film revealed a compressive yield stress of ~ 0.3 GPa, when the grain size is around 0.8 μm and the pillar diameter is 10 μm [96]. In addition, for pillars with diameters greater than grain size, the yielding is expected to be followed by an obvious working hardening arising from the grain boundary strengthening [96]. For our CG Cu, the pillars are most likely to be single crystals, because the diameter of micropillars is 1.2 μm, much smaller than its average grain size (43 μm), as shown in Fig. 1(h). Therefore, the as-received CG Cu pillars yield at a low compressive yield strength, ~ 0.2 GPa (see Table 1). After yielding, there is little work hardening in CG Cu, and the stress-displacement curves are characterized by discrete strain bursts, as shown in Fig. 5(a). Meanwhile, numerous discrete slip bands are formed on the pillar surface as shown in in Fig. 4(b1-b5), in agreement with prior studies on single-crystal metals under compression [62,71,97]. Supplementary Fig. S8 shows one typical configuration of deformed pillar for as-received CG Cu, from which the corresponding critical resolved shear stress τ_{CRSS} in slip plane is estimated to be ~ 0.1 GPa using Schmid's law. The calculated τ_{CRSS} is in good agreement with previous micropillar compression tests on (100)- or (111)-oriented single-crystal Cu pillars [74]. After irradiation, however, the upper portion of the pillar is strengthened by He bubbles and dislocation loops, so it experiences limited plastic deformation. In contrast, the lower portion is soft, and it yields first and undergoes significant plastic deformation, driven by dislocation multiplication and migration as shown in Fig. 4(c1-c5).

For the as-deposited NV-NT Cu with ultra-fine twins, dislocations are confined by TBs, and the deformation mechanism is dominated by dislocation bowing, resulting in squeezing and extrusion of the pillar top. After He irradiations at room temperature, the TBs become defective, decorated by He bubbles and SFs. These defective TBs could be stronger barriers to slip transmission via dislocations.

In order to understand the influence of SF-decorated TBs on strengthening mechanisms, MD simulations were performed for Cu with SF-decorated CTBs, as shown in Figure 10. Using the Thompson tetrahedron notation and satisfying the conservation law of Burgers vector, we describe the interactions between a dislocation and the three-layer faults. Figure 10(a) schematically illustrates the twin/matrix orientation relation and several slip systems that could be involved during deformation [98]. Start with an ideal twin boundary with the stacking sequence of … ABC<u>**A**</u>CBACB…, the three-layer fault can be formed by gliding a Shockley partial on the plane between C and B, i.e, …ABC<u>**ACA**</u>CBA … The underline indicates the fault. The Shockley partial could be one of three Burgers vectors, **A**δ′, **B**δ′, and **E**δ**’** [86]. Here, a **B**δ**’** partial dislocation glides on the (111) plane, creating the three-layer fault.

When a screw dislocation $\mathbf{b_s}$ with Burgers vector **AB** on the slip plane $(1\bar{1}1)$ moves towards the three-layer fault, as shown in Figure 10(b1), the planar-extended core condenses at the fault due to the discontinuity of slip systems in Figure 10(b2). The screw then dissociates on the secondary (111) plane (between C and A) above the original CTB in Figure 10(b3). Figure 10(b4) shows the disregistry plot of the dissociated structure with respect to the three-layer fault structure, revealing that the right partial has Burgers vector δ′**B** and the left partial has Burgers vector **A**δ**’**. The corresponding reaction can be described by **AB** = **A**δ**’** + δ′**B**. The gliding of δ′**B** partial corrects the fault, i.e., **B**δ**’** + δ′**B** = **0** in the right side of the intersection. The gliding of **A**δ′ towards the left side also corrects the fault, i.e., -(**B**δ**’** + δ′**A**) = -**BA**, corresponding to a full shear. More details on the interaction between a screw dislocation and SFs can be found in Supplementary Video SV5.

Fig. 10(c1) shows a mixed dislocation $\mathbf{b_m}$ with Burgers vector **DB** on the slip plane $(1\bar{1}1)$ moving towards the three-layer fault. Previous studies have revealed two potential reaction processes. First, **DB** = **A**$\delta'_{(CTB)}$ + **BB**$'_{(100)T}$, the slip transmission from $(1\bar{1}1)_M$ to $(100)_T$ [99]; second, **DB** = **E**$\delta'_{(CTB)}$ + **AD’**$(1\bar{1}1)_T$, the slip transmission from $(1\bar{1}1)_M$ to $(1\bar{1}1)_T$ [100]. In current case, however, the three-layer faults in Figure 10(c2) prevent the $\mathbf{b_m}$ from dissociating and transiting through the CTB. This is ascribed to the creation of a high energy SF if the dissociation occurs (see Supplementary Fig. S9). The initial fault is associated with a shear **B**δ′, and the further shear by **A**δ′ or **E**δ′ will create the high energy stacking fault, corresponding to the change in the stacking sequence from … ABC**ACA**CBA … to … ABC<u>**ACC**</u>BAC…. More details on the interaction between a mixed dislocation and SFs can be found in Supplementary Video SV6.

In summary, the SFs formed during irradiation act as strong barriers for dislocations in terms of slip transmission with different mechanisms. For a screw dislocation, the faults facilitate the cross-slip of the dislocation onto the CTB. For a mixed dislocation, the faults prevent the dissociation of the dislocation on the CTB, which enhances the energy barrier for slip transmission due to the attraction force of the residual dislocations.

Note that in Fig. 4 (d1-d5), the lower portion of the irradiated NV-NT Cu pillar did not yield preferentially as the irradiated CG Cu did in Fig. 4 (b1-b5). The Supplementary Fig. S4(c) of irradiated NV-NT Cu pillar 1 indicates that its unirradiated middle portion can sustain a higher applied stress than the pillar top when the displacement goes beyond 180 nm. This is because detwinning and softening occurred near the pillar top, while the nanotwins at the base can still provide significant strengthening, and thus preventing its preferential deformation. The retention of integrity of pillar base for NV-NT Cu could also be induced by the substrate constraints. During compression, the lower portion of the unirradiated region is constrained by the hard irradiated pillar top and the rigid Si substrate. Such constraints may develop a large friction stress along interface and strengthen the unirradiated pillar base. Similar phenomenon has been observed in Cu/amorphous-CuNb multilayers subjected to micropillar compression tests [101]. Consequently, the irradiated top portion of the NV-NT Cu micropillar first yields and undergoes significant plastic deformation. Moreover, post-compression TEM analysis has revealed significant detwinning in as-deposited NV-NT Cu, as shown in Fig. 5. Detwinning has been frequently observed in NT metals driven by migration of Shockley partials under shear stress [49,86,102–105]. In contrast, moderate detwinning occurred in He-irradiated NV-NT Cu after compression, as shown in Fig. 6. The radiation-induced He bubbles and SFs along TBs may retard detwinning and enhance strengthening in NT Cu even further.

5. Conclusions

CG and NV-NT Cu were irradiated with He ions at multiple energies to introduce a plateau of radiation damage profile, and the radiation-induced evolution of microstructures and mechanical behavior were analyzed. Our studies show that NV-NT Cu has outstanding radiation tolerance in comparison to CG Cu in terms of lower density of He bubbles and less lattice expansion. The He-irradiated NV-NT Cu reaches an ultra-high flow stress of ~1.6 GPa, one of the highest reported to date for Cu. The significant strengthening in He-irradiated NV-NT Cu arises from the defective TBs that are decorated with He bubbles and SFs. MD simulations show that SFs act as strong barriers against dislocation transmission through coherent twin boundaries. Microscopy studies also show that stress-driven detwinning is largely retarded by the He bubbles and defective TBs.

Acknowledgements

We acknowledge financial support by NSF-CMMI-1728419. C. Fan is also supported by Bilsland Dissertation Fellowship at Purdue University. Z. Shang is supported by NSF-DMR-Metallic Materials and Nanostructures Program under grant. 1611380. H. Wang acknowledges the support from the U.S. Office of Naval Research (N00014-16-1-2778). This work was performed, in part, at the Center for Integrated Nanotechnologies, an Office of Science User Facility operated for the U.S. Department of Energy (DOE) Office of Science. Los Alamos National Laboratory, an affirmative action equal opportunity employer, is managed by Triad National Security, LLC for the U.S. Department of Energy's NNSA, under contract 89233218CNA000001.

Appendix A. Supplementary data

Supplementary data to this article can be found online at https://doi.org/10.1016/j.actamat.2019.07.003.

References

[1] S. Chu, A. Majumdar, Opportunities and challenges for a sustainable energy future, Nature 488 (2012) 294–303.
[2] D. Butler, Energy: nuclear power's new dawn, Nature 429 (2004) 238–240.
[3] S.J. Zinkle, G. Was, Materials challenges in nuclear energy, Acta Mater. 61 (3) (2013) 735–758.
[4] A Technology Roadmap for Generation IV Nuclear Energy Systems, Generation IV International, Forum, 2002.
[5] GIF R&D Outlook for Generation IV Nuclear Energy Systems, Generation IV International, Forum, 2009.
[6] S.J. Zinkle, J.T. Busby, Structural materials for fission & fusion energy, Mater. Today 12 (11) (2009) 12–19.
[7] S. Zinkle, 1.03-Radiation-Induced effects on microstructure, Compr.Nucl. Mater. 1 (2012) 65–98.
[8] Z. Shang, J. Li, C. Fan, Y. Chen, Q. Li, H. Wang, T. Shen, X. Zhang, In situ study on surface roughening in radiation-resistant Ag nanowires, Nanotechnology 29 (21) (2018), 215708.
[9] D.J. Edwards, E.P. Simonen, S.M. Bruemmer, Evolution of fine-scale defects in stainless steels neutron-irradiated at 275 C, J. Nucl. Mater. 317 (1) (2003) 13–31.
[10] S. Zinkle, R. Sindelar, Defect microstructures in neutron-irradiated copper and stainless steel, J. Nucl. Mater. 155 (1988) 1196–1200.
[11] J. Li, C. Fan, J. Ding, S. Xue, Y. Chen, Q. Li, H. Wang, X. Zhang, In situ heavy ion irradiation studies of nanopore shrinkage and enhanced radiation tolerance of nanoporous Au, Sci. Rep. 7 (2017) 39484.
[12] J. Li, C. Fan, Q. Li, H. Wang, X. Zhang, In situ studies on irradiation resistance of nanoporous Au through temperature-jump tests, Acta Mater. 143 (2018) 30–42.
[13] R. Schäublin*, Z. Yao, N. Baluc, M. Victoria, Irradiation-induced stacking fault tetrahedra in fcc metals, Phil. Mag. 85 (4–7) (2005) 769–777.
[14] S. Zinkle, K. Farrell, H. Kanazawa, Microstructure and cavity swelling in reactor-irradiated dilute copper-boron alloy, J. Nucl. Mater. 179 (1991) 994–997.
[15] D. Gelles, Void swelling in binary FeCr alloys at 200 dpa, J. Nucl. Mater. 225 (1995) 163–174.
[16] D. Brimbal, B. Décamps, J. Henry, E. Meslin, A. Barbu, Single-and dual-beam in situ irradiations of high-purity iron in a transmission electron microscope: effects of heavy ion irradiation and helium injection, Acta Mater. 64 (2014) 391–401.
[17] S.J. Zinkle, Y. Matsukawa, Observation and analysis of defect cluster production and interactions with dislocations, J. Nucl. Mater. 329 (2004) 88–96.
[18] K. Yu, Y. Liu, C. Sun, H. Wang, L. Shao, E. Fu, X. Zhang, Radiation damage in helium ion irradiated nanocrystalline Fe, J. Nucl. Mater. 425 (1–3) (2012) 140–146.
[19] W.Z. Han, M.S. Ding, R.L. Narayan, Z.W. Shan, In situ study of deformation twinning and detwinning in helium irradiated small-volume copper, Adv. Eng. Mater. 19 (12) (2017) 1700357.
[20] H. Vo, A. Reichardt, D. Frazer, N. Bailey, P. Chou, P. Hosemann, In situ microtensile testing on proton beam-irradiated stainless steel, J. Nucl. Mater. 493 (2017) 336–342.
[21] Z.-J. Wang, F.I. Allen, Z.-W. Shan, P. Hosemann, Mechanical behavior of copper containing a gas-bubble superlattice, Acta Mater. 121 (2016) 78–84.
[22] A. Lupinacci, K. Chen, Y. Li, M. Kunz, Z. Jiao, G. Was, M. Abad, A. Minor, P. Hosemann, Characterization of ion beam irradiated 304 stainless steel utilizing nanoindentation and Laue microdiffraction, J. Nucl. Mater. 458 (2015) 70–76.
[23] I. Beyerlein, A. Caro, M. Demkowicz, N. Mara, A. Misra, B. Uberuaga, Radiation damage tolerant nanomaterials, Mater. Today 16 (11) (2013) 443–449.
[24] S.J. Zinkle, L.L. Snead, Designing radiation resistance in materials for fusion energy, Annu. Rev. Mater. Res. 44 (2014) 241–267.
[25] J. Silcox, P. Hirsch, Dislocation loops in neutron-irradiated copper, Phil. Mag. 4 (48) (1959) 1356–1374.
[26] A. Stathopoulos, The study of heavy-ion damage in pure copper, Philos. Mag. A 44 (2) (1981) 285–308.
[27] S.J. Zinkle, K. Farrell, Void swelling and defect cluster formation in reactor-irradiated copper, J. Nucl. Mater. 168 (3) (1989) 262–267.
[28] R. Andrievskii, Effect of irradiation on the properties of nanomaterials, Phys. Met. Metallogr. 110 (3) (2010) 229–240.
[29] Z. Fan, C. Fan, J. Li, Z. Shang, S. Xue, M.A. Kirk, M. Li, H. Wang, X. Zhang, An in situ study on Kr ion–irradiated crystalline Cu/amorphous-CuNb nanolaminates, J. Mater. Res. (2019) 1–11.
[30] L. Lu, Y. Shen, X. Chen, L. Qian, K. Lu, Ultrahigh strength and high electrical conductivity in copper, Science 304 (5669) (2004) 422–426.
[31] L. Lu, X. Chen, X. Huang, K. Lu, Revealing the maximum strength in nanotwinned copper, Science 323 (5914) (2009) 607–610.
[32] K. Lu, Stabilizing nanostructures in metals using grain and twin boundary architectures, Nat. Rev.Mater. 1 (5) (2016) 16019.
[33] Y.T. Zhu, X. Liao, Nanostructured metals: retaining ductility, Nat. Mater. 3 (6) (2004) 351.
[34] M.A. Meyers, A. Mishra, D.J. Benson, Mechanical properties of nanocrystalline materials, Prog. Mater. Sci. 51 (4) (2006) 427–556.
[35] W. Han, E. Fu, M.J. Demkowicz, Y. Wang, A. Misra, Irradiation damage of single crystal, coarse-grained, and nanograined copper under helium bombardment at 450 C, J. Mater. Res. 28 (20) (2013) 2763–2770.
[36] X. Zhang, K. Hattar, Y. Chen, L. Shao, J. Li, C. Sun, K. Yu, N. Li, M.L. Taheri, H. Wang, Radiation damage in nanostructured materials, Prog. Mater. Sci. 96 (2018) 217–321.
[37] D. Kaoumi, A. Motta, R. Birtcher, A thermal spike model of grain growth under irradiation, J. Appl. Phys. 104 (7) (2008), 073525.
[38] K. Lu, L. Lu, S. Suresh, Strengthening materials by engineering coherent internal boundaries at the nanoscale, Science 324 (5925) (2009) 349–352.
[39] Y. Shen, L. Lu, Q. Lu, Z. Jin, K. Lu, Tensile properties of copper with nano-scale twins, Scripta Mater. 52 (10) (2005) 989–994.
[40] O. Anderoglu, A. Misra, H. Wang, X. Zhang, Thermal stability of sputtered Cu films with nanoscale growth twins, J. Appl. Phys. 103 (9) (2008), 094322.
[41] Y. Chen, J. Li, K. Yu, H. Wang, M. Kirk, M. Li, X. Zhang, In situ studies on radiation tolerance of nanotwinned Cu, Acta Mater. 111 (2016) 148–156.
[42] J. Li, K. Yu, Y. Chen, M. Song, H. Wang, M. Kirk, M. Li, X. Zhang, In situ study of defect migration kinetics and self-healing of twin boundaries in heavy ion irradiated nanotwinned metals, Nano Lett. 15 (5) (2015) 2922–2927.
[43] K. Yu, D. Bufford, C. Sun, Y. Liu, H. Wang, M. Kirk, M. Li, X. Zhang, Removal of stacking-fault tetrahedra by twin boundaries in nanotwinned metals, Nat. Commun. 4 (2013) 1377.
[44] J. Li, D. Xie, S. Xue, C. Fan, Y. Chen, H. Wang, J. Wang, X. Zhang, Superior twin stability and radiation resistance of nanotwinned Ag solid solution alloy, Acta Mater. 151 (2018) 395–405.
[45] C. Fan, D. Xie, J. Li, Z. Shang, Y. Chen, S. Xue, J. Wang, M. Li, A. El-Azab, H. Wang, 9R phase enabled superior radiation stability of nanotwinned Cu alloys via in situ radiation at elevated temperature, Acta Mater. 167 (2019) 248–256.
[46] Y. Chen, K.Y. Yu, Y. Liu, S. Shao, H. Wang, M. Kirk, J. Wang, X. Zhang, Damage-tolerant nanotwinned metals with nanovoids under radiation environments, Nat. Commun. 6 (2015) 7036.
[47] C. Fan, Y. Chen, J. Li, J. Ding, H. Wang, X. Zhang, Defect evolution in heavy ion irradiated nanotwinned Cu with nanovoids, J. Nucl. Mater. 496 (2017) 293–300.
[48] C. Fan, J. Li, Z. Fan, H. Wang, X. Zhang, In situ studies on the irradiation-induced twin boundary-defect interactions in Cu, Metall. Mater. Trans. A 48 (11) (2017) 5172–5180.
[49] Y. Chen, H. Wang, M. Kirk, M. Li, J. Wang, X. Zhang, Radiation induced detwinning in nanotwinned Cu, Scripta Mater. 130 (2017) 37–41.
[50] M.J. Demkowicz, O. Anderoglu, X. Zhang, A. Misra, The influence of Σ 3 twin boundaries on the formation of radiation-induced defect clusters in nanotwinned Cu, J. Mater. Res. 26 (14) (2011) 1666–1675.
[51] G.S. Was, Fundamentals of Radiation Materials Science: Metals and Alloys, Springer, 2016.
[52] G. Was, Z. Jiao, E. Getto, K. Sun, A. Monterrosa, S. Maloy, O. Anderoglu, B. Sencer, M. Hackett, Emulation of reactor irradiation damage using ion beams, Scripta Mater. 88 (2014) 33–36.
[53] S. Zinkle, L. Snead, Opportunities and limitations for ion beams in radiation effects studies: bridging critical gaps between charged particle and neutron irradiations, Scripta Mater. 143 (2018) 154–160.
[54] P. Hosemann, Small-scale mechanical testing on nuclear materials: bridging

the experimental length-scale gap, Scripta Mater. 143 (2018) 161–168.
[55] Z. Fan, S. Zhao, K. Jin, D. Chen, Y.N. Osetskiy, Y. Wang, H. Bei, K.L. More, Y. Zhang, Helium irradiated cavity formation and defect energetics in Ni-based binary single-phase concentrated solid solution alloys, Acta Mater. 164 (2019) 283–292.
[56] W.-Z. Han, M.-S. Ding, Z.-W. Shan, Cracking behavior of helium-irradiated small-volume copper, Scripta Mater. 147 (2018) 1–5.
[57] K. Yano, M. Swenson, Y. Wu, J. Wharry, TEM in situ micropillar compression tests of ion irradiated oxide dispersion strengthened alloy, J. Nucl. Mater. 483 (2017) 107–120.
[58] Y. Zayachuk, P. Karamched, C. Deck, P. Hosemann, D.E. Armstrong, Linking microstructure and local mechanical properties in SiC-SiC fiber composite using micromechanical testing, Acta Mater. 168 (2019) 178–189.
[59] E. Aydogan, J.S. Weaver, U. Carvajal-Nunez, M.M. Schneider, J.G. Gigax, D.L. Krumwiede, P. Hosemann, T.A. Saleh, N.A. Mara, D.T. Hoelzer, Response of 14YWT alloys under neutron irradiation: a complementary study on microstructure and mechanical properties, Acta Mater. 167 (2019) 181–196.
[60] H. Vo, A. Reinhardt, D. Frazer, N. Bailey, P. Chou, P. Hosemann, In Situ Microtensile Testing for Ion Beam Irradiated Materials, Proceedings of the 18th International Conference on Environmental Degradation of Materials in Nuclear Power Systems–Water Reactors, Springer, 2019, pp. 593–603.
[61] J.F. Ziegler, M.D. Ziegler, J.P. Biersack, SRIM–The stopping and range of ions in matter, Nucl. Instrum. Methods Phys. Res. Sect. B Beam Interact. Mater. Atoms 268 (11) (2010) 1818–1823.
[62] M.D. Uchic, P.A. Shade, D.M. Dimiduk, Plasticity of micrometer-scale single crystals in compression, Annu. Rev. Mater. Res. 39 (2009) 361–386.
[63] J.R. Greer, W.C. Oliver, W.D. Nix, Size dependence of mechanical properties of gold at the micron scale in the absence of strain gradients, Acta Mater. 53 (6) (2005) 1821–1830.
[64] G. Thomas, Experimental studies of helium in metals, Radiat. Eff. 78 (1–4) (1983) 37–51.
[65] D. Chen, N. Li, D. Yuryev, J.K. Baldwin, Y. Wang, M.J. Demkowicz, Self-organization of helium precipitates into elongated channels within metal nanolayers, Sci. Adv. 3 (11) (2017), eaao2710.
[66] N. Li, M. Nastasi, A. Misra, Defect structures and hardening mechanisms in high dose helium ion implanted Cu and Cu/Nb multilayer thin films, Int. J. Plast. 32 (2012) 1–16.
[67] Y. Dai, G. Odette, T. Yamamoto, 1.06-The effects of helium in irradiated structural alloys, Compr.Nucl. Mater. (2012) 141–193.
[68] E. Fu, A. Misra, H. Wang, L. Shao, X. Zhang, Interface enabled defects reduction in helium ion irradiated Cu/V nanolayers, J. Nucl. Mater. 407 (3) (2010) 178–188.
[69] C. Fan, A. Sreekar, Z. Shang, J. Li, M. Li, H. Wang, A. El-Azab, X. Zhang, Radiation induced nanovoid shrinkage in Cu at room temperature: an in situ study, Scripta Mater. 166 (2019) 112–116.
[70] L. Mansur, W. Coghlan, Mechanisms of helium interaction with radiation effects in metals and alloys: a review, J. Nucl. Mater. 119 (1) (1983) 1–25.
[71] M.D. Uchic, D.M. Dimiduk, J.N. Florando, W.D. Nix, Sample dimensions influence strength and crystal plasticity, Science 305 (5686) (2004) 986–989.
[72] Z. Shan, R.K. Mishra, S.S. Asif, O.L. Warren, A.M. Minor, Mechanical annealing and source-limited deformation in submicrometre-diameter Ni crystals, Nat. Mater. 7 (2) (2008) 115.
[73] D. Kiener, P. Hosemann, S. Maloy, A. Minor, In situ nanocompression testing of irradiated copper, Nat. Mater. 10 (8) (2011) 608.
[74] D. Kiener, C. Motz, G. Dehm, Micro-compression testing: a critical discussion of experimental constraints, Mater. Sci. Eng. A 505 (1–2) (2009) 79–87.
[75] J.P. Wharry, K.H. Yano, P.V. Patki, Intrinsic-extrinsic size effect relationship for micromechanical tests, Scripta Mater. 162 (2019) 63–67.
[76] Q. Guo, P. Landau, P. Hosemann, Y. Wang, J.R. Greer, Helium implantation effects on the compressive response of Cu nanopillars, Small 9 (5) (2013) 691–696.
[77] X. Li, Y. Wei, L. Lu, K. Lu, H. Gao, Dislocation nucleation governed softening and maximum strength in nano-twinned metals, Nature 464 (7290) (2010) 877.
[78] M. Merz, S. Dahlgren, Tensile strength and work hardening of ultrafine-grained high-purity copper, J. Appl. Phys. 46 (8) (1975) 3235–3237.
[79] X. Zhang, H. Wang, X. Chen, L. Lu, K. Lu, R. Hoagland, A. Misra, High-strength sputter-deposited Cu foils with preferred orientation of nanoscale growth twins, Appl. Phys. Lett. 88 (17) (2006) 173116.
[80] X. Chen, L. Lu, Work hardening of ultrafine-grained copper with nanoscale twins, Scripta Mater. 57 (2) (2007) 133–136.
[81] O. Anderoglu, A. Misra, H. Wang, F. Ronning, M. Hundley, X. Zhang, Epitaxial nanotwinned Cu films with high strength and high conductivity, Appl. Phys. Lett. 93 (8) (2008), 083108.
[82] Z. You, L. Lu, K. Lu, Tensile behavior of columnar grained Cu with preferentially oriented nanoscale twins, Acta Mater. 59 (18) (2011) 6927–6937.
[83] T.-C. Liu, C.-M. Liu, H.-Y. Hsiao, J.-L. Lu, Y.-S. Huang, C. Chen, Fabrication and characterization of (111)-oriented and nanotwinned Cu by Dc electrodeposition, Cryst. Growth Des. 12 (10) (2012) 5012–5016.
[84] Z. You, X. Li, L. Gui, Q. Lu, T. Zhu, H. Gao, L. Lu, Plastic anisotropy and associated deformation mechanisms in nanotwinned metals, Acta Mater. 61 (1) (2013) 217–227.
[85] A. Misra, J. Hirth, R. Hoagland, Length-scale-dependent deformation mechanisms in incoherent metallic multilayered composites, Acta Mater. 53 (18) (2005) 4817–4824.
[86] J. Wang, N. Li, O. Anderoglu, X. Zhang, A. Misra, J. Huang, J. Hirth, Detwinning mechanisms for growth twins in face-centered cubic metals, Acta Mater. 58 (6) (2010) 2262–2270.
[87] Z. Hu, J. Du, P. Wang, X. Wang, Y. Zhang, Y. Qiu, E. Fu, Insight into the impact of nanovoids on the electrical and mechanical properties of nanotwinned copper films, Scripta Mater. 137 (2017) 41–45.
[88] G. Lucas, The evolution of mechanical property change in irradiated austenitic stainless steels, J. Nucl. Mater. 206 (2–3) (1993) 287–305.
[89] U. Kocks, The relation between polycrystal deformation and single-crystal deformation, Metall. Mater. Trans. B 1 (5) (1970) 1121–1143.
[90] W. Han, M. Demkowicz, E. Fu, Y. Wang, A. Misra, Effect of grain boundary character on sink efficiency, Acta Mater. 60 (18) (2012) 6341–6351.
[91] N. Hashimoto, T. Byun, K. Farrell, S. Zinkle, Deformation microstructure of neutron-irradiated pure polycrystalline metals, J. Nucl. Mater. 329 (2004) 947–952.
[92] M.-S. Ding, J.-P. Du, L. Wan, S. Ogata, L. Tian, E. Ma, W.-Z. Han, J. Li, Z.-W. Shan, Radiation-induced helium nanobubbles enhance ductility in submicron-sized single-crystalline copper, Nano Lett. 16 (7) (2016) 4118–4124.
[93] M.-S. Ding, L. Tian, W.-Z. Han, J. Li, E. Ma, Z.-W. Shan, Nanobubble fragmentation and bubble-free-channel shear localization in helium-irradiated submicron-sized copper, Phys. Rev. Lett. 117 (21) (2016), 215501.
[94] F. Kroupa, P. Hirsch, Elastic interaction between prismatic dislocation loops and straight dislocations, Discuss. Faraday Soc. 38 (1964) 49–55.
[95] R. Stoller, S. Zinkle, On the relationship between uniaxial yield strength and resolved shear stress in polycrystalline materials, J. Nucl. Mater. 283 (2000) 349–352.
[96] M. Mutoh, T. Nagoshi, T.-F.M. Chang, T. Sato, M. Sone, Micro-compression test using non-tapered micro-pillar of electrodeposited Cu, Microelectron. Eng. 111 (2013) 118–121.
[97] A.T. Jennings, M.J. Burek, J.R. Greer, Microstructure versus size: mechanical properties of electroplated single crystalline Cu nanopillars, Phys. Rev. Lett. 104 (13) (2010), 135503.
[98] N. Li, J. Wang, A. Misra, X. Zhang, J. Huang, J. Hirth, Twinning dislocation multiplication at a coherent twin boundary, Acta Mater. 59 (15) (2011) 5989–5996.
[99] J. Wang, H. Huang, Novel deformation mechanism of twinned nanowires, Appl. Phys. Lett. 88 (20) (2006) 203112.
[100] Z.-H. Jin, P. Gumbsch, K. Albe, E. Ma, K. Lu, H. Gleiter, H. Hahn, Interactions between non-screw lattice dislocations and coherent twin boundaries in face-centered cubic metals, Acta Mater. 56 (5) (2008) 1126–1135.
[101] Z. Fan, Q. Li, J. Li, S. Xue, H. Wang, X. Zhang, Tailoring plasticity of metallic glasses via interfaces in Cu/amorphous CuNb laminates, J. Mater. Res. 32 (14) (2017) 2680–2689.
[102] Y. Liu, J. Jian, Y. Chen, H. Wang, X. Zhang, Plasticity and ultra-low stress induced twin boundary migration in nanotwinned Cu by in situ nanoindentation studies, Appl. Phys. Lett. 104 (23) (2014), 231910.
[103] D. Bufford, Y. Liu, J. Wang, H. Wang, X. Zhang, In situ nanoindentation study on plasticity and work hardening in aluminium with incoherent twin boundaries, Nat. Commun. 5 (2014) 4864.
[104] K.Y. Yu, D. Bufford, F. Khatkhatay, H. Wang, M.A. Kirk, X. Zhang, In situ studies of irradiation induced twin boundary migration in nanotwinned Ag, Scripta Mater. 69 (2013) 385.
[105] J. Wang, A. Misra, J. Hirth, Shear response of Σ 3 {112} twin boundaries in face-centered-cubic metals, Phys. Rev. B 83 (6) (2011), 064106.